

Article

State of Health Estimation of Lithium-Ion Batteries Using Fusion Health Indicator by PSO-ELM Model

Jun Chen ¹, Yan Liu ¹, Jun Yong ², Cheng Yang ³, Liqin Yan ³  and Yanping Zheng ^{1,*} 

¹ College of Automobile and Traffic Engineering, Nanjing Forestry University, Nanjing 210037, China; cuidonglin@njfu.edu.cn (J.C.); ly8221611622@njfu.edu.cn (Y.L.)

² State Grid Dangtu County Power Supply Company, Maanshan 243100, China; jy36767377@outlook.com

³ State Key Laboratory of Space Power-Sources, Shanghai Institute of Space Power-Sources, Shanghai 200245, China; yangcheng_811@sina.com (C.Y.); yanlq@163.com (L.Y.)

* Correspondence: zhengyp@njfu.com.cn; Tel.: +86-138-5186-4173

Abstract: The accurate estimation of the State of Health (SOH) of lithium-ion batteries is essential for ensuring their safe and reliable operation, as direct measurement is not feasible. This paper presents a novel SOH estimation method that integrates Particle Swarm Optimization (PSO) with an Extreme Learning Machine (ELM) to improve prediction accuracy. Health Indicators (HIs) are first extracted from the battery's charging curve, and correlation analysis is conducted on seven indirect HIs using Pearson and Spearman coefficients. To reduce dimensionality and eliminate redundancy, Principal Component Analysis (PCA) is applied, with the principal component contributing over 94% used as a fusion HI to represent battery capacity degradation. PSO is then employed to optimize the weights (ϵ) between the input and hidden layers, as well as the hidden layer bias (u) in the ELM, treating these parameters as particles in the PSO framework. This optimization enhances the ELM's performance, addressing instability issues in the standard algorithm. The proposed PSO-ELM model demonstrates superior accuracy in SOH prediction compared with ELM and other methods. Experimental results show that the mean absolute error (MAE) is 0.0034, the mean absolute percentage error (MAPE) is 0.467%, and the root mean square error (RMSE) is 0.0043, providing a valuable reference for battery safety and reliability assessments.



Citation: Chen, J.; Liu, Y.; Yong, J.; Yang, C.; Yan, L.; Zheng, Y. State of Health Estimation of Lithium-Ion Batteries Using Fusion Health Indicator by PSO-ELM Model. *Batteries* **2024**, *10*, 380. <https://doi.org/10.3390/batteries10110380>

Academic Editor: Rodolfo Dufo-López

Received: 19 September 2024

Revised: 14 October 2024

Accepted: 25 October 2024

Published: 28 October 2024



Copyright: © 2024 by the authors. Licensee MDPI, Basel, Switzerland. This article is an open access article distributed under the terms and conditions of the Creative Commons Attribution (CC BY) license (<https://creativecommons.org/licenses/by/4.0/>).

1. Introduction

Electric vehicles (EVs) are progressively replacing traditional fossil fuel-based internal combustion engine vehicles, offering an effective means to reduce emissions of CO₂, nitrogen oxides, and sulfur dioxide [1,2]. As the primary energy source for EVs, the performance of the power battery directly influences the power, economy, safety, and service life of these vehicles [3]. However, over long-term usage, batteries inevitably experience aging and potential failure [4]. The main indicators of this degradation include attenuation of battery capacity, increase in internal resistance, intensification of self-discharge, and decline in power performance. Severely aged batteries can also lead to spontaneous combustion, fires, or explosions, posing significant risks to vehicle performance and personal safety [5]. Therefore, accurate estimation of the State of Health (SOH) of batteries is crucial for safety and reliability assessments, failure warnings, effective maintenance, and tiered utilization.

Battery SOH, defined as the ratio of a battery's actual capacity to its initial rated capacity, is typically expressed as a percentage. Currently, the primary methods for estimating SOH can be categorized into three main approaches: direct measurement, model-based, and data-driven methods. The direct measurement approach assesses the current health status of the battery through its capacity and internal resistance, yielding relatively accurate results [6]. Pecht's method of measuring battery capacity across 800 cycles at temperatures from 25 °C to 40 °C is well justified [7]. However, this kind of method could only be carried

out in laboratory conditions in an offline mode [8]. Chen et al. [9] proposed an online SOH estimation method for lithium-ion batteries based on the linear relationship between ohmic internal resistance and capacity fade, achieving a high-precision SOH assessment through two discharge tests at different aging stages. Due to the requirement for specific equipment, direct measurement methods are typically conducted in laboratory settings and are often time-consuming [10], limiting their practicality in engineering applications. The model-based approach primarily estimates battery SOH through online identification of the battery's equivalent circuit model [11–13] or electrochemical model parameters [14–16]. Chen et al. [17] presented an online battery health condition evaluation technique based on model parameters to determine diffusion-controlled capacitance, to estimate parameters using a genetic algorithm, and to derive an equation for SOH calculation. Xu et al. [18] considered the impact of time-varying temperature conditions on lithium-ion battery discharge capacity and aging law, proposing a stochastic degradation rate model based on the Arrhenius temperature model and an aging model under varying temperatures using the Wiener process. Lui et al. [19] proposed a physics-based approach to predict lithium-ion battery capacity by modeling degradation mechanisms such as active material losses of positive and negative electrodes and lithium inventory loss. However, the effectiveness of model-based methods is limited by the model's credibility and robustness [20,21].

The battery SOH can also be estimated online using data-driven methods, which offer high accuracy and flexibility. In data-driven methods, the battery system is treated as a black-box model, eliminating the need to account for the complex internal mechanisms of the battery [22]. As battery data accumulate, data-driven methods have gained traction in engineering due to their inherent advantages. In SOH estimation, commonly used data-driven methods include neural networks [23,24], support vector machines [25], Gaussian process regression [26], among others, and are often combined with intelligent algorithms [27,28]. Feng S et al. [29] proposed a multi-source information fusion method based on a Gaussian mixture model and Bayesian inference distance for the health assessment of vehicle batteries. Since battery charge–discharge data are essentially time series, current sampled data are influenced by previous samples. To extract the nonlinearity and time-series correlation in the data, neural networks are introduced due to their diverse hidden layer structures [30,31]. Specifically, Recurrent Neural Networks (RNNs) account for the influence of previous time information on current measurements [32] but suffer from issues like gradient vanishing and explosion during model training [33]. To overcome the limitations of Recurrent Neural Networks (RNNs) [34,35], Long Short-Term Memory (LSTM) has been applied to battery SOH estimation [27], effectively preventing issues such as gradient vanishing and explosion. Its simplified alternative, Gated Recurrent Units (GRUs), offers similar advantages with reduced computational complexity, enabling efficient battery SOH estimation without compromising accuracy [36,37]. Additionally, Physics-Informed Neural Networks (PINNs) [38,39] have emerged as a powerful data-driven approach. By integrating physical models with deep learning, PINNs can achieve high accuracy with limited data, enhancing model stability and generalization. Wang et al. [40] proposed a method using PINNs that integrates physical equations governing battery dynamics into the neural network training process. Thelen et al. [41] combined physics-based modeling and machine learning to diagnose battery degradation, demonstrating robust performance across different battery types and conditions. Despite these advancements, challenges remain, including the complexity of physical models and the difficulty in obtaining internal parameters.

In addition to these neural network approaches, the Extreme Learning Machine (ELM) has also been explored for use in battery SOH estimation [42,43]. Unlike RNNs, LSTM, and GRUs, which require iterative training and careful tuning of hyperparameters, an ELM is a single-layer feedforward neural network that randomly initializes the input weights and biases and only needs to solve for the output weights using a least squares solution [44]. This simplicity and computational efficiency make ELMs particularly suitable for real-time applications and scenarios with limited computational resources. Chen et al. [45]

introduced a novel Metabolic Extreme Learning Machine (M-ELM) framework designed to capture the intricate mechanisms of battery degradation, effectively reflecting the most recent degradation trends. Ma et al. [46] proposed a Broad Learning-ELM (BL-ELM) approach, where feature and enhancement nodes are combined to form a new input layer, thereby reducing computational time, and improving efficiency. Ge et al. [47] improved the ELM using the Bat Algorithm (BA) to enhance the estimation accuracy of the SOH of lithium-ion batteries, achieving a Root Mean Square Error (RMSE) of 0.5354% and a Mean Absolute Error (MAE) of 0.4326%. To leverage the strengths of different algorithms, the development of hybrid methods combining an ELM with other optimization techniques has emerged as a new research direction.

Data-driven battery SOH estimation requires two key techniques: extraction of Health Indicators (HIs) to evaluate SOH, and development of a suitable data-driven algorithm [48,49]. HIs can be classified into direct and indirect indicators, which are extracted from measured parameters under varying degrees of battery aging. These indicators have a specific coupling relationship with the battery's current capacity and reflect its degree of aging. Direct HIs, such as battery capacity and internal resistance, directly reflect the battery's aging level. However, obtaining direct HIs is time-consuming and cannot be performed in real-time, making the extraction of indirect HIs from monitorable state parameters a hot research topic. Indirect HIs are typically extracted from charging and discharging data, using characteristic parameters that strongly correlate with battery aging. For example, Zhou Y et al. [50] used the mean value of discharge voltage changes as an indirect HI to characterize the aging state of the battery. Wu J et al. [51] utilized the difference in terminal voltage during charging across different cycles as an indirect HI. Since data from the discharge stage are heavily influenced by external factors, indirect HIs extracted from the charging stage are more applicable in practical engineering contexts.

In light of the above, this study derives several indirect health indicators associated with battery capacity degradation for use in multi-indicator fusion and correlation analysis, focusing on the charging stage. The Extreme Learning Machine (ELM) is optimized using Particle Swarm Optimization (PSO) to estimate the SOH of lithium-ion batteries.

2. Extraction and Fusion of Health Indicators

2.1. Battery Data Source

This study investigates battery SOH using publicly available data sets for the 18650 Model B0005, B0006, B0007, and B0018, provided by NASA's Prognostics Center of Excellence (PCoE). The datasets are based on commercial 18650-type lithium-ion batteries, with lithium cobalt oxide (LiCoO_2) as the cathode material and graphite as the anode material. The batteries underwent multiple charge–discharge cycles at a constant temperature of approximately 24 °C. Figure 1 illustrates the capacity degradation curve for each cycle of the four battery groups.

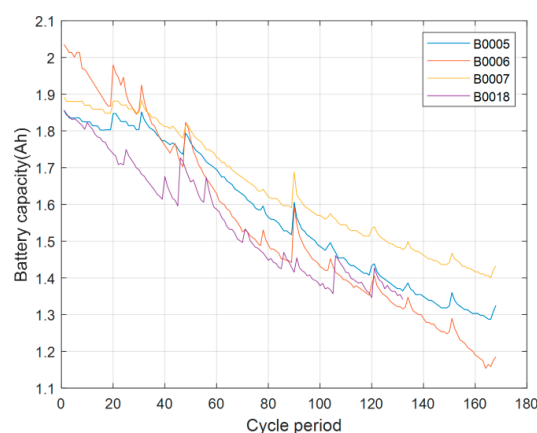


Figure 1. Battery capacity decline curve.

2.2. Extraction of Health Indicators

This study focuses on external data from the battery charging stage to select and analyze the battery's health indicators. Using the B0005 battery as an example, we analyze the current, voltage, and temperature data during the charging stage. The variations in voltage, current, temperature, and Incremental Capacity (IC) across different cycles are shown in Figure 2.

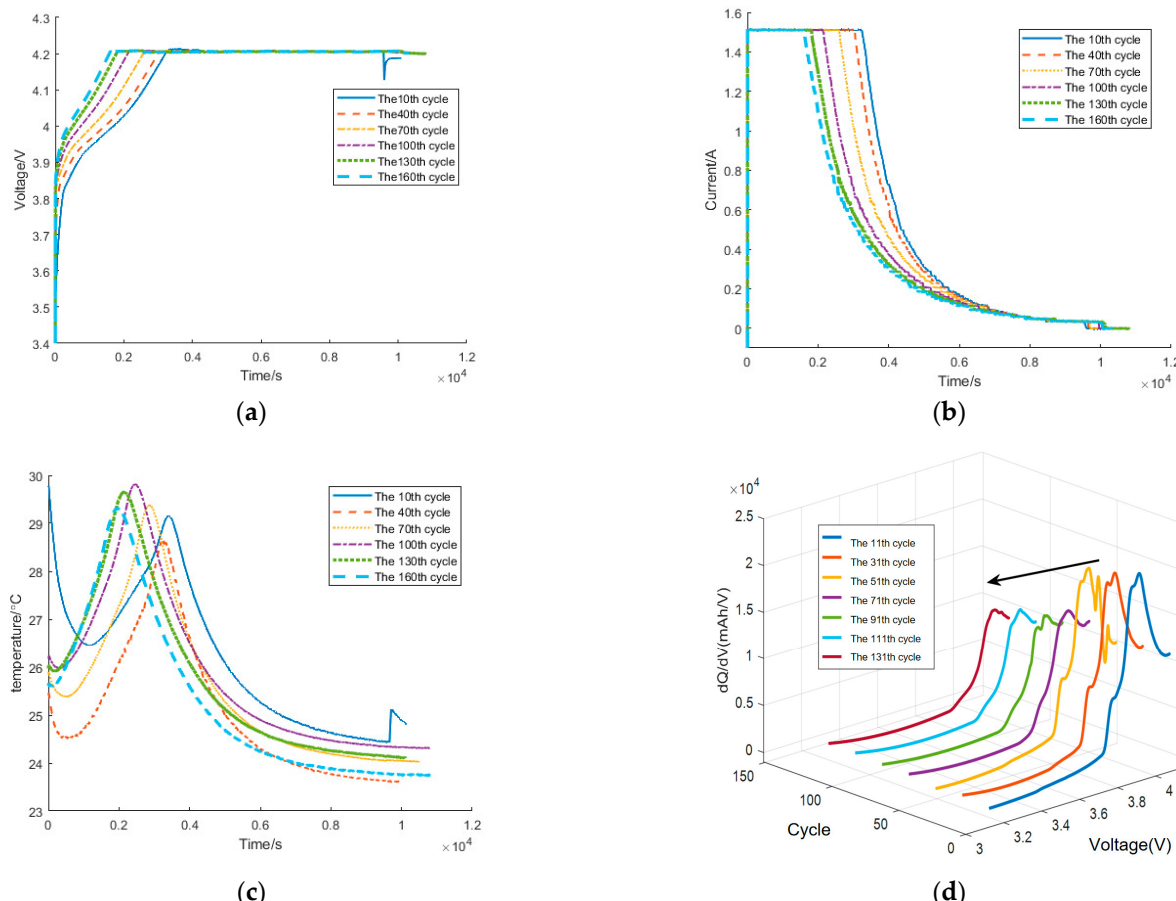


Figure 2. Changes in external data of the battery: (a) Voltage; (b) Electric currents; (c) Temperature; (d) Battery capacity increment.

According to Figure 2a, the constant current charging time decreases with an increasing number of cycles, indicating a reduction in the time required to reach the charging cut-off voltage of 4.2 V and an increased rate of voltage change during the constant current charging period. Therefore, the relationship between voltage variation characteristics and battery capacity degradation can be analyzed by examining the time consumption within the same voltage variation interval or the voltage change within the same time interval. As shown in Figure 2b, the constant current charging time decreases as the cycle period increases, suggesting that less charge can be stored and that battery polarization deepens, both impacting the battery's SOH. As observed in Figure 2c, the battery's temperature decreases briefly before rising continuously. After reaching the maximum temperature, it gradually decreases, and the time to reach peak temperature shortens as the cycle period increases. Figure 2d demonstrates that with increasing cycle periods, the peak of the IC curve gradually decreases and shifts towards higher voltage.

By systematically analyzing the current, voltage, and temperature data during the charging stage, we extracted several key indirect health indicators, each of which is closely tied to the trends observed in Figure 2. For example, the voltage interval charging time at 3.8–4.2 V, as shown in Figure 2a, decreases with each cycle, reflecting a reduction in the

battery's ability to retain charge. The constant current charging time, depicted in Figure 2b, also shortens as the cycle count increases, indicating diminished energy storage capacity and increased battery polarization. The average voltage increase within 1000–1500 s, as indicated in Figure 2c, rises as the cycle progresses, providing insight into the voltage changes that occur during the constant current charging phase. The current difference after a 1500 s interval similarly reflects the impact of aging on the charging process. Additionally, the IC value at 4 V, corresponding to the peak of the IC curve, can be observed shifting toward higher voltages and decreasing in magnitude in Figure 2d, highlighting battery polarization and capacity fading. The voltage corresponding to the peak of the IC curve also shifts, further illustrating the degradation process. Lastly, the time to reach maximum temperature, observed in Figure 2c, becomes shorter as cycles increase, indicating a change in the battery's thermal behavior as it ages. The variations of these seven indirect health indicators across different cycles are depicted in Figure 3a–g.

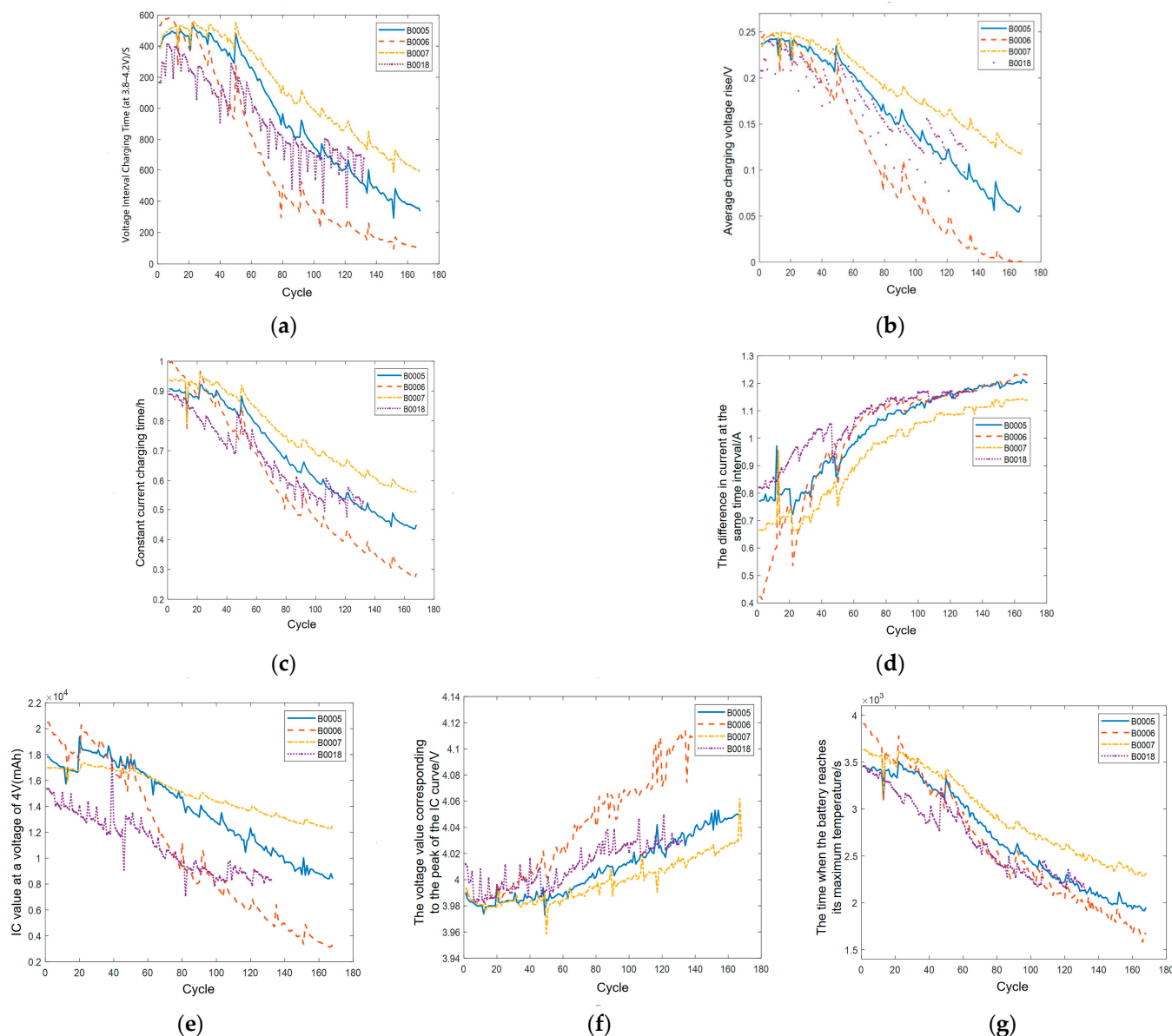


Figure 3. Indirect health indicators: (a) Voltage interval charging time at 3.8–4.2 V; (b) Average charging voltage rise; (c) Constant current charging time; (d) The difference in current at the same time interval; (e) IC value at a voltage of 4 V; (f) The voltage value corresponding to the peak of the IC curve; (g) The time when the battery reaches its maximum temperature.

2.3. Correlation Analysis and Multi-Index Fusion

To further analyze the correlation between indirect health indicators and battery capacity degradation, this study employs both Pearson and Spearman correlation coefficients. The Pearson correlation coefficient r measures the strength of the linear relationship between two variables, with values ranging from -1 to 1 . The larger the absolute value, the stronger the correlation. The Spearman correlation coefficient ρ assesses whether the relationship between two variables is strictly monotonic, with values also ranging from -1 to 1 . Similarly, a larger absolute value indicates a stronger monotonic relationship.

The extracted indicators—including the voltage interval charging time at 3.8–4.2 V, average charging voltage rise, constant current charging time, current difference at the same time interval, IC value at 4 V, voltage corresponding to the peak IC value, and the time when the battery reaches its maximum temperature—are represented by HI-1 to HI-7. The specific meanings of these indirect health indicators are listed in Table 1, while their Pearson and Spearman correlation coefficients with battery capacity are shown in Table 2.

Table 1. Indirect health indicator number and meaning.

Number	Number Meaning	Number	Number Meaning
HI-1	Voltage interval charging time at 3.8–4.2 V	HI-5	The IC value at a voltage of 4 V
HI-2	Average charging voltage rise	HI-6	The voltage value corresponding to the peak of the IC curve
HI-3	Constant current charging time	HI-7	The time when the battery reaches its maximum temperature
HI-4	The current drops from 1.5 A to the current difference at intervals of 1500 s		

Table 2. Correlation analysis between indirect health indicators and volume.

Health Indicators	B0005		B0006		B0007		B0018	
	r	ρ	r	ρ	r	ρ	r	ρ
HI-1	0.9921	0.9779	0.9481	0.9528	0.9128	0.9375	0.8192	0.8837
HI-2	0.9765	0.9592	0.9546	0.9610	0.8914	0.9467	0.7956	0.8788
HI-3	0.9387	0.9543	0.9519	0.9569	0.9010	0.9527	0.8474	0.9173
HI-4	-0.9687	-0.9923	-0.8985	-0.9544	-0.9279	-0.9526	-0.8905	-0.9278
HI-5	0.9839	0.9763	0.9423	0.9542	0.8710	0.9501	0.7915	0.9008
HI-6	-0.9696	-0.9670	-0.9689	-0.9860	-0.9053	-0.9272	-0.8542	-0.8632
HI-7	0.9268	0.9543	0.9371	0.9558	0.9924	0.9865	0.8468	0.9312

As shown in Table 2, there is a strong correlation between the seven extracted indirect health indicators and battery capacity, with HI-4 and HI-6 showing negative correlations, while the others are positively correlated. The Pearson correlation coefficients r for HI-2 and HI-5 in the B0018 battery range from 0.7 to 0.8, indicating a strong correlation with the capacity of this specific battery. The correlation coefficients r and ρ for the remaining five health indicators are all greater than 0.8, indicating a strong correlation with battery capacity. This analysis demonstrates that the seven extracted indirect HIs effectively characterize battery capacity degradation and can serve as reliable indicators.

However, the analysis reveals issues of information overlap and high dimensionality among the seven extracted indirect HIs. To reduce data dimensionality and computational complexity, this study employs Principal Component Analysis (PCA) to fuse the seven indirect HIs. PCA maps original high-dimensional data into a lower-dimensional space via linear transformation, retaining as much information as possible in the principal components, significantly reducing dimensionality, and eliminating noise. The calculation process is as follows.

- (1) Let the sample matrix be $X_{m \times n}$, where m is the number of samples and n is the number of feature parameters. To eliminate the influence of different dimensions of the feature parameters, each feature parameter needs to be standardized, as shown in Equation (1).

$$\bar{x}_{ij} = \frac{x_{ij} - \bar{x}_j}{n_j} \quad (i = 1, 2, \dots, m; j = 1, 2, \dots, n) \quad (1)$$

In the equation, \bar{x}_{ij} is the standardized characteristic parameter; \bar{x}_j and n_j are the sample mean and standard deviation of the j -th characteristic parameter, respectively.

- (2) To find the correlation coefficient matrix R , the calculation formulas are as follows: Equations (2) and (3).

$$R = (r_{ij})_{m \times n} \quad (2)$$

$$r_{ij} = \frac{\sum_{k=1}^m \bar{x}_{ki} \cdot \bar{x}_{kj}}{m-1} \quad (i = 1, 2, \dots, m; j = 1, 2, \dots, n) \quad (3)$$

In the equation, $r_{ii} = 1$, $r_{ij} = r_{ji}$, r_{ij} is the correlation coefficient between the i -th feature parameter and the j -th feature parameter.

- (3) Calculate the eigenvalues $\lambda = [\lambda_1, \lambda_2, \lambda_3, \dots, \lambda_n]$ of the correlation coefficient matrix R and the eigenvectors $\omega = [\omega_1, \omega_2, \omega_3, \dots, \omega_n]$ corresponding to the eigenvalues.
(4) The contribution rate C_i and cumulative contribution rate C of each feature are calculated according to Equations (4) and (5) respectively.

$$C_i = \frac{\lambda_i}{\sum_{i=0}^n \lambda_i} \quad i = 1, 2, \dots, n \quad (4)$$

$$C = \frac{\sum_{i=0}^p \lambda_i}{\sum_{i=0}^n \lambda_i} \quad p = 1, 2, \dots, n \quad (5)$$

Table 3 presents each principal component and its corresponding contribution rate, derived from the PCA analysis of the seven indirect HIs.

Table 3. Contribution rates of each principal component.

Battery Number	First Principal Component (%)	Second Principal Component (%)	Third Principal Component (%)	Fourth Principal Component (%)	Fifth Principal Component (%)	Sixth Principal Component (%)	Seventh Principal Component (%)
B0005	95.5054	2.4220	1.5451	0.3280	0.1450	0.0459	0.0066
B0006	96.4459	2.4936	0.7397	0.2180	0.0729	0.0235	0.0063
B0007	94.7197	3.1280	1.8262	0.2236	0.0648	0.0301	0.0074
B0018	94.0327	3.5084	1.2114	1.0145	0.1842	0.0353	0.0136

As shown in Table 3, the contribution rate of the first principal component for each of the four battery groups exceeds 94%. Therefore, the first principal component is selected for further correlation analysis. In Figure 4a–d, the x-axis represents the battery capacity, while the y-axis represents the first principal component for each battery. The scatter plots indicate a clear linear relationship between the x-axis and y-axis, demonstrating a strong positive correlation between the first principal component and battery capacity. Table 4 presents the Pearson and Spearman correlation coefficients between the first principal component and battery capacity.

As shown in Table 4, the Pearson correlation coefficients between the first principal component and battery capacity for the four groups are 0.9901, 0.9602, 0.9863, and 0.8607, respectively, while the Spearman correlation coefficients are 0.9844, 0.9606, 0.9770, and 0.9085, respectively. Both Pearson and Spearman correlation coefficients are superior to

the indirect HI correlation coefficients shown in Table 2. Therefore, the first principal component is chosen as the fusion HI for subsequent research on battery SOH estimation.

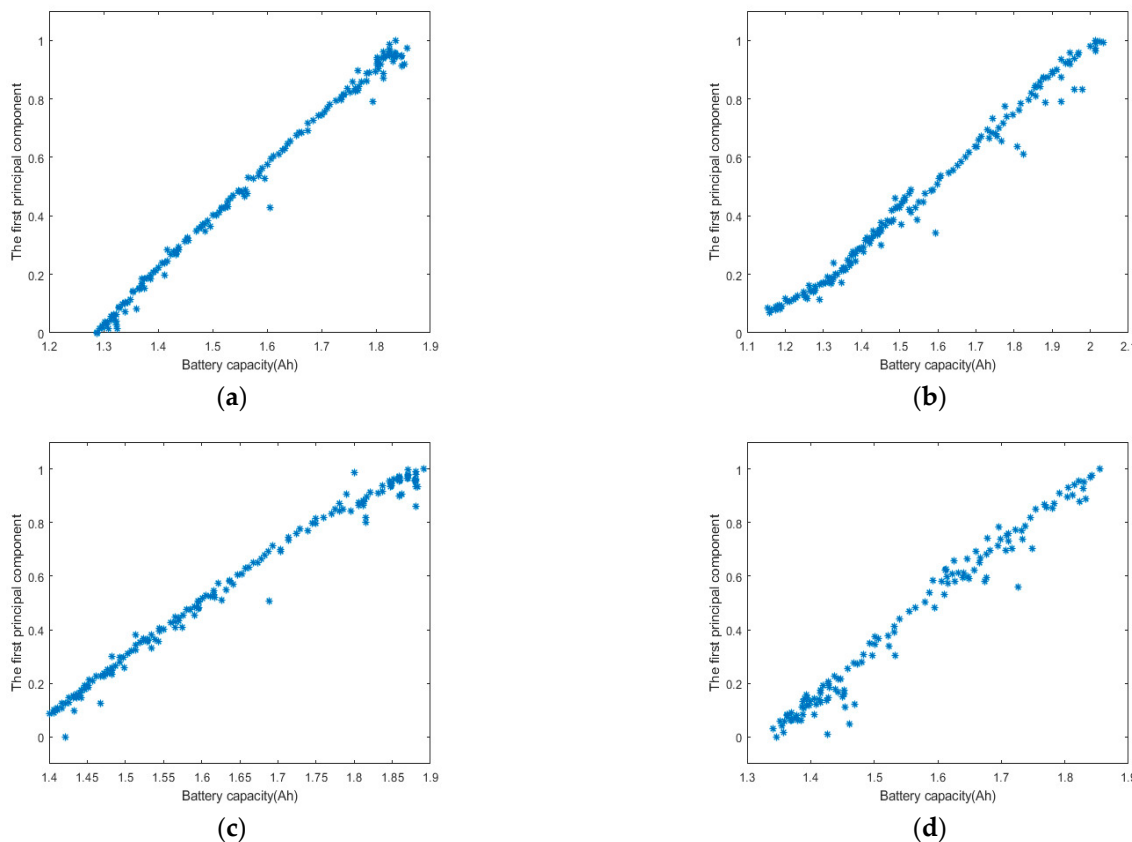


Figure 4. Scatter diagram of the relationship between the first principal component and the capacity of each battery. (a) B0005, (b) B0006, (c) B0007, (d) B0018.

Table 4. Correlation analysis between the first principal component and battery capacity.

Battery Number	First Principal Component	
	r	ρ
B0005	0.9901	0.9844
B0006	0.9602	0.9606
B0007	0.9863	0.9770
B0018	0.8607	0.9085

3. Particle Swarm Optimization Optimizes Extreme Learning Machine

The particle swarm optimization (PSO) algorithm is commonly used to optimize the parameters of other algorithms [52]. This paper employs PSO to enhance the Extreme Learning Machine (ELM) for online estimation of battery SOH using the fusion health indicator. PSO is applied to optimize the weights and biases of the Extreme Learning Machine (ELM) model. By treating these parameters as particles, PSO enhances the stability and accuracy of the ELM in the SOH estimation of lithium-ion batteries.

3.1. Extreme Learning Machine

Due to the issues of long training duration, slow training speed, and poor generalization performance in traditional feedforward neural network models [53], Huang Guangbin et al. proposed the method of the Extreme Learning Machine (ELM). The core concept of the ELM involves adding a hidden layer between the input and output layers and randomly initializing the connection weights and biases of the hidden layer nodes. The

ELM approach produces an efficient classification or regression model by employing either the regularized least squares method or the pseudo-inverse matrix solution. The network structure is illustrated in Figure 5.

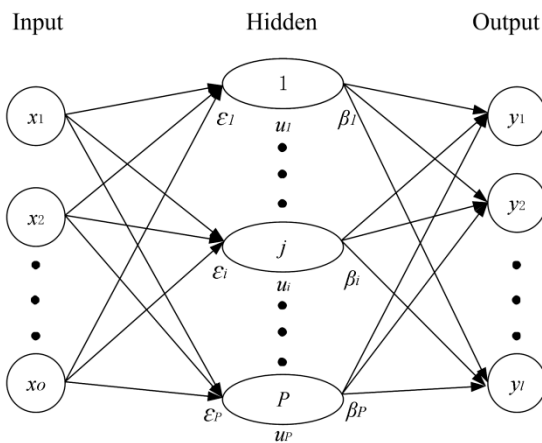


Figure 5. ELM network structure.

In Figure 5, the input and output of the training sample set are set as follows: $I = \{x_i, y_i\}$, dimension is $o \times l$, x_i is o -dimensional input feature vector, y_i is l -dimensional output vector, number of training samples is Q , and P is the number of hidden layer nodes contained in the ELM, whose value is less than Q . According to the ELM network training in Figure 5, the output is shown in Equation (6),

$$y_i = \sum_{j=1}^P \beta_j g(\varepsilon_j \cdot x_i + u_j), \quad i = 1, 2, \dots, Q; \quad j = 1, 2, \dots, P \quad (6)$$

where $g(\cdot)$ is the activation function of neurons in the hidden layer, $\varepsilon_j \cdot x_i$ is the inner product of ε_j and x_i ; $\{\varepsilon_j\}$ is the input weight between the input layer and the hidden layer node; $\{u_j\}$ is the hidden layer node deviation; and $\{\beta_j\}$ is the output weight between the output layer and the hidden layer node.

The corresponding matrix form is shown in Equation (7),

$$Y = H \cdot \beta \quad (7)$$

where Y is the output matrix, is the value output matrix of $P \times l$, and H is the output matrix of the hidden layer. Its specific expression is shown in Equations (8)–(10).

$$H(\varepsilon_1, \dots, \varepsilon_P, x_1, \dots, x_Q, u_1, \dots, u_p) = \begin{bmatrix} g(\varepsilon_1 \cdot x_1 + u_1) & \cdots & g(\varepsilon_P \cdot x_1 + u_P) \\ \vdots & \ddots & \vdots \\ g(\varepsilon_1 \cdot x_Q + u_1) & \cdots & g(\varepsilon_P \cdot x_Q + u_P) \end{bmatrix} \quad (8)$$

$$\beta = [\beta_1^T \quad \beta_2^T \quad \cdots \quad \beta_P^T]^T \quad (9)$$

$$Y = [y_1^T \quad y_2^T \quad \cdots \quad y_Q^T]^T \quad (10)$$

In order to enhance the generalization of the ELM, it is recommended that the ELM be trained using the minimum output weight norm and training error. This will enable the minimum norm least square solution $\tilde{\beta} = H^+ W$ to yield the output weight β of the hidden layer. According to the definition of the Moore–Penrose generalized inverse matrix, Equation (11) is used to further solve the weight matrix β .

$$\tilde{\beta} = (H^T \cdot H)^{-1} \cdot H^T \cdot W \quad (11)$$

Equation (11) states that the input weight ε and deviation u are used to train the ELM model, and that the training process of the ELM model concludes when the output weight β is solved.

3.2. PSO-Optimized ELM Implementation Process

The complex collinearity issues in the ELM can lead to unstable prediction outcomes and reduced accuracy, particularly when there is a linear relationship between the randomly generated input weight ε and the deviation u [54]. Therefore, Particle Swarm Optimization (PSO) is introduced in this paper to optimize the weight ε between the input layer and the hidden layer of the ELM, and the deviation u of the hidden layer. The approach involves treating ε and u as particles of PSO to develop an optimized ELM prediction model. This optimization addresses the issue of unstable prediction performance in the ELM algorithm. The PSO-optimized ELM implementation process is illustrated in Figure 6.

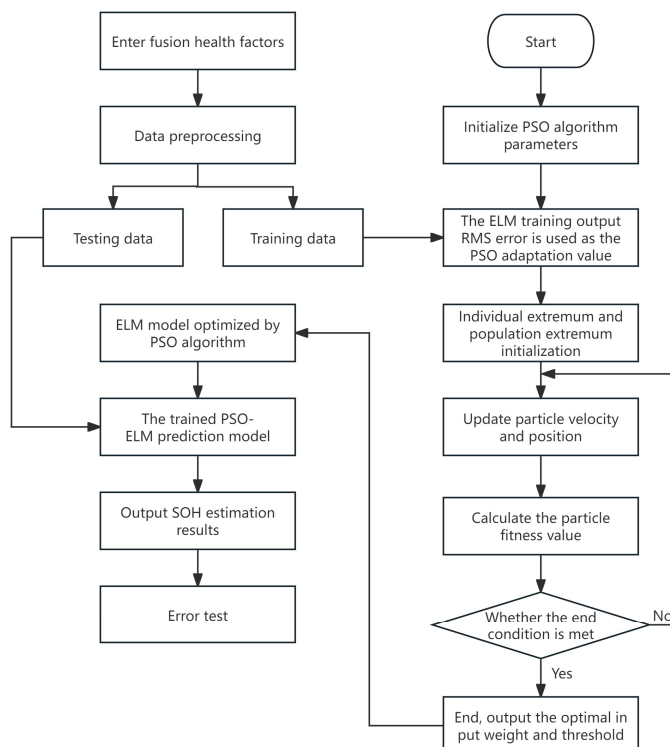


Figure 6. PSO-optimized ELM implementation process.

The update rule of the PSO algorithm involves initializing a set of random particles and iteratively searching for optimal solutions by locating individual and global extrema to update particle positions. In each iteration, particles update their velocity and position based on individual best positions and the global best position, with the updated equations provided in Equations (12) and (13):

$$v_{id}^{t+1} = \omega v_{id}^t + c1r1(p_{id}^t - x_{id}^t) + c2r2(p_{gd}^t - x_{id}^t) \quad (12)$$

$$x_{id}^{t+1} = x_{id}^t + v_{id}^{t+1} \quad (13)$$

where ω is the inertia weight; $c1$ and $c2$ are non-negative learning factors; $r1$ and $r2$ are random numbers between 0 and 1; v_{id}^t is the velocity of the i -th particle at time t ; x_{id}^t is the position of the i -th particle in the solution space at time t ; p_{id}^t is the optimal solution of the i -th particle until time t ; and p_{gd}^t is the global optimal solution for all particles up to k iterations.

4. Lithium-Ion Battery SOH Estimates

To intuitively evaluate the estimation accuracy of the PSO-ELM model for battery SOH, the Mean Absolute Error (MAE), Root Mean Square Error (RMSE), and Mean Absolute Percentage Error (MAPE) are used as evaluation indicators to predict the outcome.

- (1) MAE is calculated as the average of the absolute differences between predicted and actual values. MAE avoids the issue of errors cancelling each other out, thus providing a more accurate reflection of the actual prediction error. A smaller MAE indicates a smaller difference between the predicted and actual values, suggesting better model performance. The calculation of MAE is given by Equation (14):

$$\text{MAE} = \frac{1}{n_e} \sum_{i=1}^{n_e} |\text{SOH}(i) - \tilde{\text{SOH}}(i)| \quad (14)$$

where n_e is the number of test cases, $\text{SOH}(i)$ is the actual SOH value of the battery at the i -th cycle, and $\tilde{\text{SOH}}(i)$ is the predicted SOH value of the battery at the i -th cycle.

- (2) RMSE is primarily used to measure the deviation between predicted and actual values. It is calculated by taking the square root of the average of the squared differences between predicted and actual values. A smaller RMSE indicates a smaller difference between the predicted and actual values, implying higher prediction accuracy. The calculation of RMSE is given by Equation (15):

$$\text{RMSE} = \sqrt{\frac{1}{n_e} \sum_{i=1}^{n_e} (\text{SOH}(i) - \tilde{\text{SOH}}(i))^2} \quad (15)$$

- (3) MAPE expresses the error size as a percentage and is commonly used to evaluate the prediction accuracy of time series models. A MAPE of 0% indicates a perfect model, while a MAPE of 100% indicates a poor model. The calculation of MAPE is given by Equation (16):

$$\text{MAPE} = \frac{100\%}{n_e} \sum_{i=1}^{n_e} \left| \frac{\text{SOH}(i) - \tilde{\text{SOH}}(i)}{\text{SOH}(i)} \right| \quad (16)$$

In this paper, the integrated health indicators are used as the input of the PSO-ELM model, and the battery SOH is used as the output to establish an online estimation model for battery SOH. The parameters are set as follows: the incentive function of the hidden layer of the ELM neural network selects the “sigmoid” function, and the number of nodes in the hidden layer is set to 6. In the PSO algorithm, the maximum population size is 100, the maximum number of iterations is set to 100, the learning factor $c1 = 0.8$, $c2 = 1.7$, the maximum value of the inertia factor is 1, and the minimum value is 0.6. Taking B0005 and B0007 batteries as examples, the standard ELM algorithm and the PSO-ELM algorithm are used to train and test the health indicators of battery fusion, respectively. When the prediction starting point is 80, the estimation results and error results of the two algorithms are shown in Figure 7a–d.

To objectively evaluate the effectiveness of the PSO-ELM algorithm for battery SOH estimation, this study compares its estimation errors with those of the unoptimized Extreme Learning Machine (ELM) algorithm, the Least Squares Support Vector Machine (LSSVM) model as referenced in [55], the Gaussian Process Regression optimized by Particle Swarm Algorithm (PSO-GPR) as referenced in [56], the standard Long Short-Term Memory (LSTM) network, and the Long Short-Term Memory optimized by Particle Swarm Algorithm (PSO-LSTM) as referenced in [57]. The comparison results are presented in Table 5.

As can be seen from Figure 7, compared with the ELM algorithm, most of the errors in the estimation of battery SOH by the PSO-ELM model fluctuate in the range of $[-0.01, +0.01]$, and the estimation errors and error fluctuation amplitudes are smaller. In addition, it can be seen from Table 5 that for the SOH estimation results of the B0005 battery, the MAE, MAPE, and RMSE based on the PSO-ELM algorithm are reduced by

0.013, 1.90%, and 0.0169, respectively, compared with those based on a single ELM. For the SOH estimation result of the B0007 battery, the MAE, MAPE, RMSE based on the PSO-ELM algorithm are reduced by 0.0128, 1.67%, and 0.0133, respectively, compared with that of a single ELM. Furthermore, the PSO-ELM model also demonstrates significant advantages over LSSVM, PSO-GPR, LSTM, and PSO-LSTM, showing lower MAE, MAPE, and RMSE values. Consequently, the PSO-ELM algorithm demonstrates higher accuracy, reduced error margins, and more stable estimation results for battery SOH estimation.

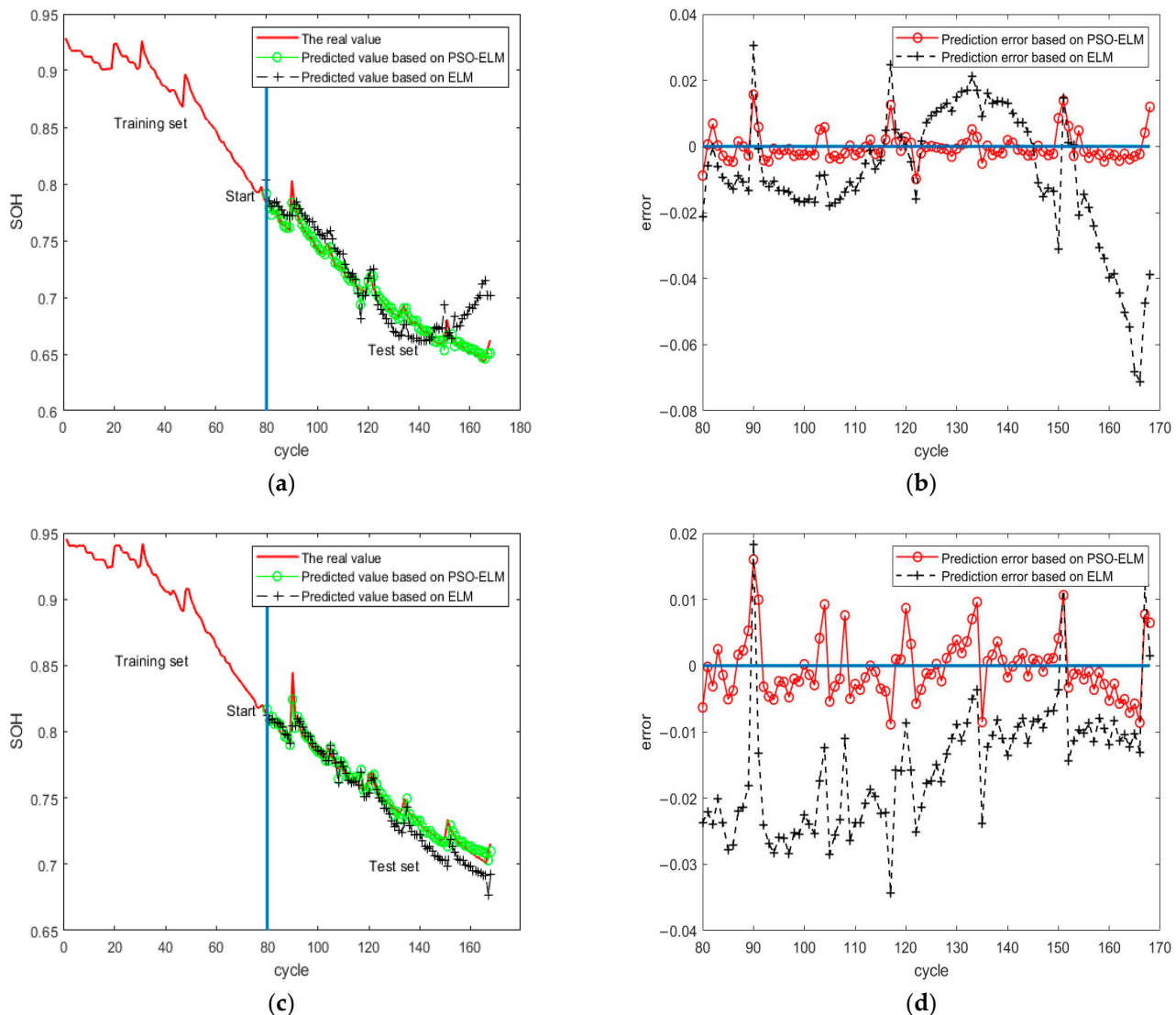


Figure 7. SOH estimation results and error comparison of batteries B0005 and B0007. (a) B0005 Battery estimation result, (b) B0005 Battery error comparison, (c) B0007 Battery estimation result, (d) B0007 Battery error comparison.

Table 5. Evaluation of SOH estimation error results of B0005 and B0007 batteries.

Error	Algorithm	MAE		MAPE (%)		RMSE	
		B0005	B0007	B0005	B0007	B0005	B0007
PSO-ELM	PSO-ELM	0.0031	0.0036	0.44	0.47	0.0043	0.0046
	ELM	0.0161	0.0164	2.34	2.14	0.0212	0.0179
LSSVM [55]	PSO-ELM	0.0037	0.0047	-	-	0.0047	0.0057
PSO-GPR [56]	PSO-ELM	0.0063	0.0058	-	-	0.0069	0.0078
LSTM [57]	PSO-ELM	0.0235	0.0181	3.24	2.36	0.0268	0.0224
PSO-LSTM [57]	PSO-ELM	0.0126	0.0102	1.74	1.31	0.0140	0.0112

5. Comparative Analysis of the Characterization Results of Health Indicators

To verify the effectiveness of the fusion health indicators in characterizing battery SOH, according to the correlation analysis results in Table 2, the three most correlated indirect health indicators, HI-1(Voltage Interval Charging Time at 3.8–4.2 V), HI-2(Average charging voltage rise), and HI-5(IC value at a voltage of 4 V), were selected as inputs for the PSO-ELM model. A test set was employed to evaluate the battery SOH characterization using both fusion health indicators and multiple indirect health indicators, respectively.

Generally, the data from the first 60% to 70% of the cycles within the battery life threshold are used as the training set, and the last 30% to 40% are used as the test set. Due to the battery Remaining Useful Life (RUL) prediction, a study will be carried out in the future. The failure threshold of B0005, B0006, and B0008 batteries is around 120. The failure threshold of B0018 battery failure threshold is around 90. Therefore, the prediction starting point was set at 80 for B0005, B0006, and B0007 batteries, and at 60 for the B0018 battery.

The SOH of B0005, B0006, B0007, and B0018 batteries was characterized using the PSO-ELM algorithm based on the three selected indirect health indicators and the fusion health indicator. The estimated results and corresponding errors of the two methods are presented in Figures 8–11.

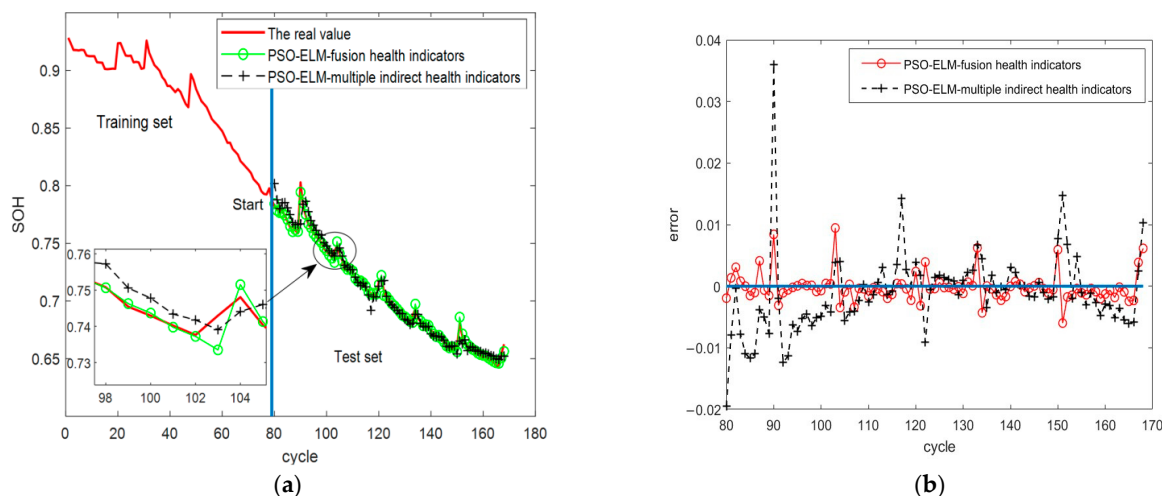


Figure 8. Comparison of SOH characterization results and errors of B0005 battery by different health indicators. (a) Characterization results, (b) Comparison of errors.

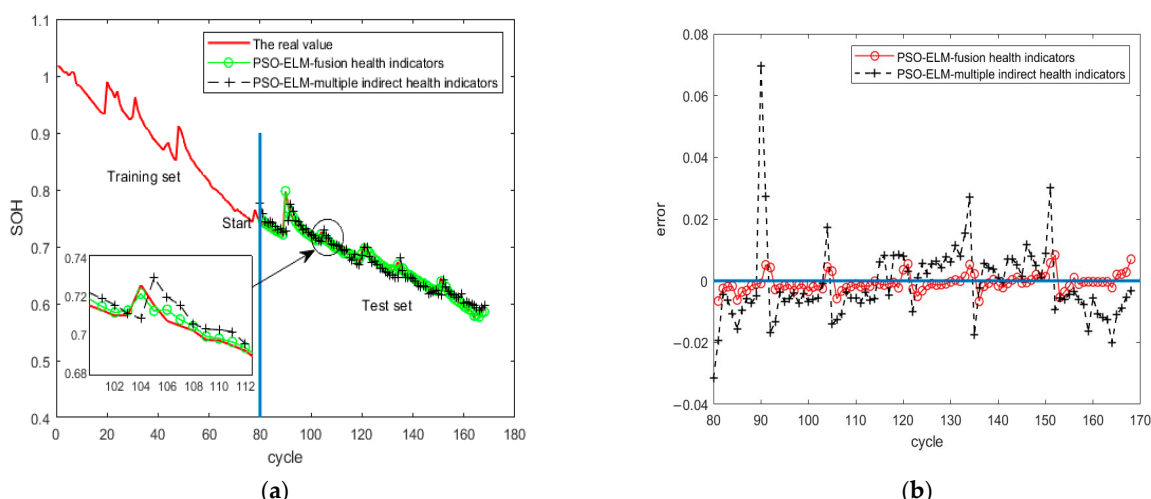


Figure 9. Comparison of SOH characterization results and errors of B0006 battery by different health indicators. (a) Characterization results, (b) Comparison of errors.

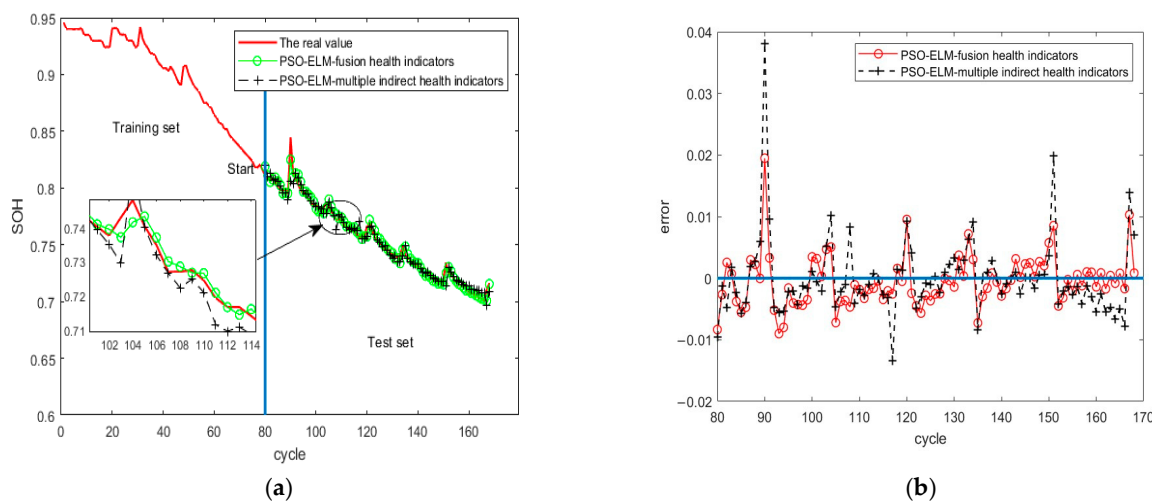


Figure 10. Comparison of SOH characterization results and errors of B0007 battery by different health indicators. (a) Characterization results, (b) Comparison of errors.

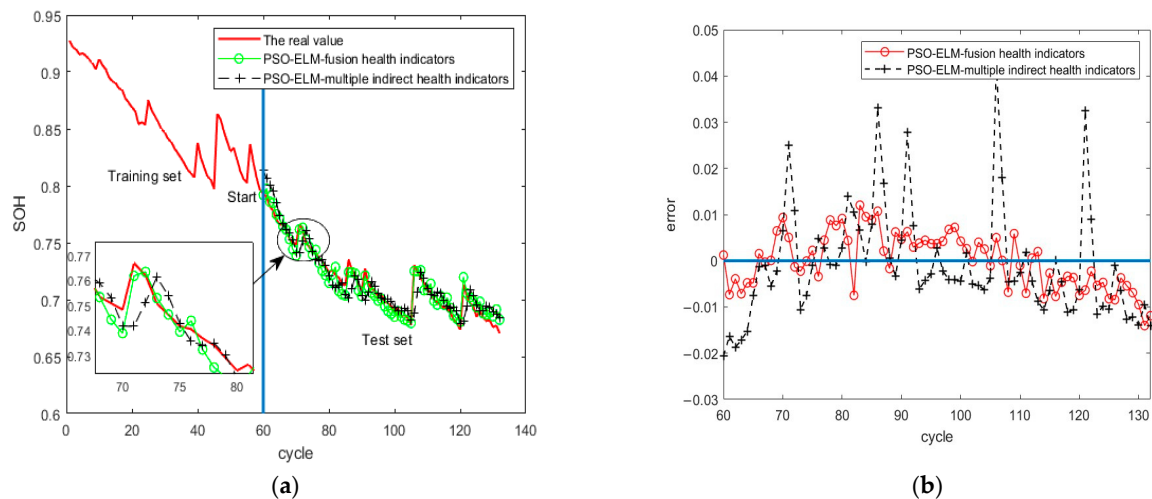


Figure 11. Comparison of SOH characterization results and errors of B0018 battery by different health indicators. (a) Characterization results, (b) Comparison of errors.

As shown in Figures 8–11, both fusion health indicators and multiple indirect health indicators serve as inputs and effectively characterize the battery SOH. However, regarding error range, the errors obtained using fusion health indicators are generally within 0.01 to -0.01 , with minimal fluctuations. Errors from multiple indirect health indicators also generally fall within this range, though some exceed it. The error results indicate that SOH characterization based on fusion health indicators is more stable compared to using multiple health indicators, with stronger tracking effects during specific capacity regeneration cycles, such as the 90th cycle. This stability is attributed to the ability of fusion health indicators to better characterize the battery's health state by retaining distinctive information from each indirect health indicator while eliminating noise, unlike multiple indirect health indicators that suffer from high-dimensional issues and information overlap.

As shown in Table 6, the MAE, MAPE, and RMSE for the B0005 battery SOH based on integrated health indicators are 0.0032, 0.42%, and 0.0038, respectively, while those obtained using multiple health indicators are 0.0064, 0.63%, and 0.0068, respectively. Both the MAE and RMSE values derived from fusion and multiple health indicators are under 0.01, with MAPE values also being relatively low. Therefore, the PSO-ELM model effectively characterizes battery SOH using both multiple health indicators and the fusion health indicator. However, the MAE and RMSE values derived from multiple indirect

health indicators are approximately double those of the integrated health indicators, and the MAPE is also consistently higher. Additionally, the training and estimation times are longer when using multiple indirect health indicators compared to the fusion health indicator. With large training datasets, both training time and complexity significantly increase. Similar results were obtained for B0006, B0007, and B0018 batteries, where different health indicators yielded consistent characterization results. Thus, the research findings suggest that the fusion health indicator offers superior SOH characterization with faster training and estimation times.

Table 6. Comparison of battery SOH characterization results by different health indicators.

Battery Number	Health Indicators	Training Time (s)	Estimated Time (s)	MAE	MAPE (%)	RMSE
B0005	Fusion health indicators	27.9863	0.0034	0.0032	0.42	0.0038
	Multiple indirect health indicators	31.8802	0.0045	0.0064	0.63	0.0068
B0006	Fusion health indicators	26.8932	0.0033	0.0019	0.33	0.0032
	Multiple indirect health indicators	31.1125	0.0038	0.0128	1.34	0.0128
B0007	Fusion health indicators	27.0581	0.0029	0.0034	0.41	0.0043
	Multiple indirect health indicators	33.1283	0.0037	0.0046	0.53	0.0046
B0018	Fusion health indicators	18.9031	0.0019	0.0051	0.71	0.0059
	Multiple indirect health indicators	23.7633	0.0025	0.0088	1.22	0.0120

6. Conclusions

This paper proposes a method for estimating the SOH of lithium-ion batteries using a PSO-ELM approach. To validate the effectiveness of the PSO-ELM algorithm, NASA lithium-ion battery test data were utilized to compare SOH estimation results across the PSO-ELM, ELM, LSSVM, PSO-GPR, LSTM, and PSO-LSTM methods.

This study indicates that the PSO-ELM model estimates the SOH of B0005 and B0007 batteries with MAE, MAPE, and RMSE values of 0.0031, 0.44%, 0.0043; and 0.0036, 0.47%, 0.0046, respectively. These values represent decreases of 0.013, 1.90%, and 0.0169; and 0.0128, 1.67%, and 0.0133, respectively, compared to a single ELM. Compared to the standard ELM method, the PSO-ELM model yields more stable and accurate SOH estimations. Furthermore, the PSO-ELM model also demonstrates significant advantages over LSSVM, PSO-GPR, LSTM, and PSO-LSTM, showing lower MAE, MAPE, and RMSE values. When comparing fusion health indicators with multiple indirect health indicators for SOH characterization using the PSO-ELM model, results show that for B0005, B0006, B0007, and B0018 batteries, the MAE, MAPE, and RMSE based on fusion health indicators are 0.0031, 0.21%, 0.003; 0.0109, 1.01%, 0.0096; 0.0012, 0.12%, 0.0003; and 0.0037, 0.51%, 0.0061, respectively, all of which are lower than those based on multiple indirect health indicators. Additionally, the use of fusion health indicators results in shorter training and estimation times, facilitating rapid and precise SOH estimation.

The analysis in this paper is based entirely on experimental data, and the proposed method has yet to be validated in real-world engineering applications. Under practical operating conditions, dynamic adjustments to the health indicators may be required.

The indirect health indicators considered in this study are extracted during battery charging. Future work should incorporate the complex and variable dynamic operating conditions of the battery into the prediction model, including factors like charging rate, external temperature fluctuations, and varying initial charging capacities.

Author Contributions: Conceptualization, J.C. and Y.Z.; methodology, Y.Z.; software, J.C.; validation, Y.L., J.Y. and C.Y.; formal analysis, L.Y.; resources, Y.Z.; data curation, J.C.; writing—original draft preparation, J.C.; writing—review and editing, Y.Z.; supervision, Y.Z. All authors have read and agreed to the published version of the manuscript.

Funding: This research was funded by the State Key Laboratory of Space Power-Sources fund project.

Data Availability Statement: The data presented in this study are available on request from the corresponding author.

Conflicts of Interest: Author Jun Yong was employed by the State Grid Dangtu County Power Supply Company. The remaining authors declare that the research was conducted in the absence of any commercial or financial relationships that could be construed as a potential conflict of interest.

References

1. Kumar, R.R.; Alok, K. Adoption of electric vehicle: A literature review and prospects for sustainability. *Clean. Prod.* **2020**, *253*, 119911. [[CrossRef](#)]
2. Guo, J.; Zhang, X.; Gu, F.; Zhang, H.; Fan, Y. Does air pollution stimulate electric vehicle sales? Empirical evidence from twenty major cities in China. *Clean. Prod.* **2020**, *249*, 119372. [[CrossRef](#)]
3. Xie, Y.; Jiang, D.; Zhang, Y.J.; Li, W.; Yang, R.; Qian, Y. Joint estimation algorithm of SOC-SOP for lithium-ion battery pack in new energy vehicles. *J. Automot. Saf. Energy* **2022**, *13*, 580–589.
4. Wu, S.J.; Yuan, X.D.; Xu, Q.S.; Chen, B.; Li, Q. Review on lithium-ion battery health state assessment. *Chin. J. Power Sources* **2017**, *41*, 1788–1791.
5. Jiang, J.C.; Gao, Y.; Zhang, C.P.; Wang, Y.B.; Zhang, W.; Liu, S.J. Online Diagnostic Method for Health Status of Lithium-ion Battery in Electric Vehicle. *J. Mech. Eng.* **2019**, *55*, 60–72,84.
6. Hu, X.; Jiang, J.; Cao, D.; Egardt, B. Battery Health Prognosis for Electric Vehicles Using Sample Entropy and Sparse Bayesian Predictive Modeling. *IEEE Trans. Ind. Electron.* **2016**, *63*, 2645–2656. [[CrossRef](#)]
7. Lee, T.-Y.; Chen, N. Optimal Capacity of the Battery Energy Storage System in a Power System. *IEEE Trans. Energy Convers.* **1993**, *8*, 667–673.
8. You, G.; Park, S.; Oh, D. Real-Time State-of-Health Estimation for Electric Vehicle Batteries: A Data-Driven Approach. *Appl. Energy* **2016**, *176*, 92–103. [[CrossRef](#)]
9. Chen, L.; Lü, Z.; Lin, W.; Li, J.; Pan, H. A New State-of-Health Estimation Method for Lithium-Ion Batteries through the Intrinsic Relationship between Ohmic Internal Resistance and Capacity. *Measurement* **2018**, *116*, 586–595. [[CrossRef](#)]
10. Xiong, R.; Li, L.; Tian, J. Towards a Smarter Battery Management System: A Critical Review on Battery State of Health Monitoring Methods. *J. Power Sources* **2018**, *405*, 18–29. [[CrossRef](#)]
11. Andre, D.; Nuhic, A.; Soczka-Guth, T.; Sauer, D.U. Comparative study of a structured neural network and an extended Kalman filter for state of health determination of lithium-ion batteries in hybrid electric vehicles. *Eng. Appl. Artif. Intell.* **2013**, *26*, 951–961. [[CrossRef](#)]
12. Li, C.; Cui, N.; Cui, Z.; Wang, C.; Zhang, C. Novel equivalent circuit model for high energy lithium-ion batteries considering the effect of nonlinear solid-phase diffusion. *J. Power Sources* **2022**, *523*, 230993. [[CrossRef](#)]
13. Wang, L.; Han, J.; Liu, C.; Li, G. State of charge estimation of Lithium-ion based on VFFRLS-noise adaptive CKF algorithm. *Ind. Eng. Chem. Res.* **2022**, *61*, 7489–7503. [[CrossRef](#)]
14. Hosseiniinasab, S.; Lin, C.; Pischinger, S.; Stapelbroek, M.; Vagnoni, G. State-of-health estimation of lithium-ion batteries for electrified vehicles using a reduced-order electrochemical model. *J. Energy Storage* **2022**, *52*, 104684. [[CrossRef](#)]
15. Wang, D.; Zhang, Q.; Huang, H.; Yang, B.; Dong, H.; Zhang, J. An electrochemical–thermal model of lithium-ion battery and state of health estimation. *J. Energy Storage* **2022**, *47*, 103528. [[CrossRef](#)]
16. Xu, Z.; Wang, J.; Lund, P.D.; Zhang, Y. Co-estimating the state of charge and health of lithium batteries through combining a minimalist electrochemical model and an equivalent circuit model. *Energy* **2022**, *240*, 122815. [[CrossRef](#)]
17. Chen, Z.; Mi, C.C.; Fu, Y.; Xu, J.; Gong, X. Online battery state of health estimation based on Genetic Algorithm for electric and hybrid vehicle applications. *J. Power Sources* **2013**, *240*, 184–192. [[CrossRef](#)]
18. Xu, X.; Tang, S.; Yu, C.; Xie, J.; Han, X.; Ouyang, M. Remaining useful life prediction of lithium-ion batteries based on Wiener process under time-varying temperature condition. *Reliab. Eng. Syst. Saf.* **2021**, *214*, 107675. [[CrossRef](#)]
19. Lui, Y.H.; Li, M.; Downey, A.; Shen, S.; Nemanic, V.P.; Ye, H.; VanElzen, C.; Jain, G.; Hu, S.; Laflamme, S.; et al. Physics-based prognostics of implantable-grade lithium-ion battery for remaining useful life prediction. *J. Power Sources* **2021**, *485*, 229327. [[CrossRef](#)]
20. Xu, C.; Li, L.W.; Yang, Y.X. State of Health Estimation of Lithium-Ion Battery Based on Improved Particle Filter. *J. Automob. Technol.* **2020**, *12*, 19–24.
21. Sun, S.S.; Hou, Y.; Gong, X.L. Research of the accelerated fatigue experiment method based on the particle filtering algorithm method and the theory of crack growth. *Theor. Appl. Fract. Mech.* **2023**, *124*, 103746.
22. Liu, L.J.; Gao, Y.Z.; Zhu, J.Z.; Zhang, X. Data-driven SOH estimation of Li-ion battery. *Battery Bimon.* **2022**, *52*, 157–161.

23. Wang, F.; Zhao, Z.; Zhai, Z.; Guo, Y.; Xi, H.; Wang, S.; Chen, X. Feature disentanglement and tendency retainment with domain adaptation for lithium-ion battery capacity estimation. *Reliab. Eng. Syst. Saf.* **2023**, *230*, 108897. [[CrossRef](#)]
24. Luo, K.; Chen, X.; Zheng, H.; Shi, Z. A review of deep learning approach to predicting the state of health and state of charge of lithium-ion batteries. *J. Energy Chem.* **2022**, *74*, 159–173. [[CrossRef](#)]
25. Nuhic, A.; Terzimehic, T.; Soczka-Guth, T.; Buchholz, M.; Dietmayer, K. Health diagnosis and remaining useful life prognostics of lithium-ion batteries using data-driven methods. *J. Power Sources* **2013**, *239*, 680–688. [[CrossRef](#)]
26. Richardson, R.R.; Osborne, M.A.; Howey, D.A. Gaussian process regression for forecasting battery state of health. *J. Power Sources* **2017**, *357*, 209–219. [[CrossRef](#)]
27. Wang, S.L.; Wu, F.; Takyi-Aninakwa, P.; Fernandez, C.; Stroe, D.I.; Huang, Q. Improved singular filtering-Gaussian process regression-long short-term memory model for whole-life-cycle remaining capacity estimation of lithium-ion batteries adaptive to fast aging and multi-current variations. *Energy* **2023**, *284*, 128677. [[CrossRef](#)]
28. Ding, D.; Sun, N.; Li, A.; Li, Z.; Zhang, Y. Research on vehicle battery data cleaning method based on OOA-VMD-ATGRU-GAN. *Phys. Scr.* **2024**, *99*, 045013. [[CrossRef](#)]
29. Feng, S.; Wang, A.; Cai, J.; Zuo, H.; Zhang, Y. Health State Estimation of On-Board Lithium-Ion Batteries Based on GMM-BID Model. *Sensors* **2022**, *22*, 9637. [[CrossRef](#)]
30. Manoharan, A.; Begam, K.M.; Aparow, V.R.; Sooriamoorthy, D. Artificial neural networks, gradient boosting and support vector machines for electric vehicle battery state estimation: A review. *J. Energy Storage* **2022**, *55*, 105384. [[CrossRef](#)]
31. Ren, Y.M.; Alhajeri, M.S.; Luo, J.; Chen, S.; Abdullah, F.; Wu, Z.; Christofides, P.D. A tutorial review of neural network modeling approaches for model predictive control. *Comput. Chem. Eng.* **2022**, *165*, 107956. [[CrossRef](#)]
32. Elman, J.L. Finding structure in time. *Cogn. Sci.* **1990**, *14*, 179–211. [[CrossRef](#)]
33. Li, Z.; Bai, F.; Zuo, H.; Zhang, Y. Remaining Useful Life Prediction for Lithium-Ion Batteries Based on Iterative Transfer Learning and Mogrifier LSTM. *Batteries* **2023**, *9*, 448. [[CrossRef](#)]
34. Teixeira, R.S.D.; Calili, R.F.; Almeida, M.F.; Louzada, D.R. Recurrent neural networks for estimating the state of health of lithium-ion batteries. *Batteries* **2024**, *10*, 111. [[CrossRef](#)]
35. Chen, Z.; Zhao, H.; Zhang, Y.; Shen, S.; Shen, J.; Liu, Y. State of health estimation for lithium-ion batteries based on temperature prediction and gated recurrent unit neural network. *J. Power Sources* **2022**, *521*, 230892. [[CrossRef](#)]
36. Guo, F.; Zhu, S.; Huang, G.; Deng, S.; Wang, R.; Jiang, J.; Yan, H.; Lin, R. Optimized GRU based on satin bowerbird algorithm for lithium-ion battery state of health estimation. In Proceedings of the 2023 5th International Conference on Power and Energy Technology (ICPET), Tianjin, China, 27–30 July 2023; pp. 349–353.
37. Huo, F.; Chen, C.-H. The state of charge estimation based on GRU for lithium-ion batteries. In Proceedings of the 2022 IEEE 11th Global Conference on Consumer Electronics (GCCE), Osaka, Japan, 18–21 October 2022; pp. 220–221.
38. Chen, Z.; Liu, Y.; Sun, H. Physics-informed learning of governing equations from scarce data. *Nat. Commun.* **2021**, *12*, 6136. [[CrossRef](#)]
39. Karniadakis, G.E.; Kevrekidis, I.G.; Lu, L.; Perdikaris, P.; Wang, S.; Yang, L. Physics-informed machine learning. *Nat. Rev. Phys.* **2021**, *3*, 422–440. [[CrossRef](#)]
40. Wang, F.; Zhai, Z.; Zhao, Z.; Di, Y.; Chen, X. Physics-informed neural network for lithium-ion battery degradation stable modeling and prognosis. *Nat. Commun.* **2024**, *15*, 4332. [[CrossRef](#)]
41. Thelen, A.; Lui, Y.H.; Shen, S.; Laflamme, S.; Hu, S.; Ye, H.; Hu, C. Integrating physics-based modeling and machine learning for degradation diagnostics of lithium-ion batteries. *Energy Storage Mater.* **2022**, *50*, 668–695. [[CrossRef](#)]
42. Pan, H.; Lü, Z.; Wang, H.; Wei, H.; Chen, L. Novel battery state-of-health online estimation method using multiple health indicators and an extreme learning machine. *Energy* **2018**, *160*, 466–477. [[CrossRef](#)]
43. Razavi-Far, R.; Chakrabarti, S.; Saif, M.; Zio, E.; Palade, V. Extreme learning machine based prognostics of battery life. *Int. J. Artif. Intell. Tools* **2018**, *27*, 1850036. [[CrossRef](#)]
44. Luo, X.; Sun, J.; Wang, L.; Wang, W.; Zhao, W.; Wu, J. Short-term wind speed forecasting via stacked extreme learning machine with generalized correntropy. *IEEE Trans. Ind. Inform.* **2018**, *14*, 4963–4971. [[CrossRef](#)]
45. Chen, L.; Wang, H.; Liu, B.; Wang, Y.; Ding, Y.; Pan, H. Battery state-of-health estimation based on a metabolic extreme learning machine combining degradation state model and error compensation. *Energy* **2021**, *215*, 78–88. [[CrossRef](#)]
46. Ma, Y.; Wu, L.; Guan, Y.; Peng, Z. The capacity estimation and cycle life prediction of lithium-ion batteries using a new broad extreme learning machine approach. *J. Power Sources* **2020**, *476*, 228581. [[CrossRef](#)]
47. Ge, D.; Zhang, Z.; Kong, X.; Wan, Z. Extreme learning machine using bat optimization algorithm for estimating state of health of lithium-ion batteries. *Appl. Sci.* **2022**, *12*, 1398. [[CrossRef](#)]
48. Hu, X.S.; Che, Y.H.; Lin, X.K.; Onori, S. Battery health prediction using fusion-based feature selection and machine learning. *IEEE Trans. Transp. Electrif.* **2021**, *7*, 382–398. [[CrossRef](#)]
49. Li, Z.; Li, A.; Bai, F.; Zuo, H.; Zhang, Y. Remaining useful life prediction of lithium battery based on ACNN-Mogrifier LSTM-MMD. *Meas. Sci. Technol.* **2023**, *35*, 016101. [[CrossRef](#)]
50. Zhou, Y.; Huang, M.; Chen, Y.; Tao, Y. A novel health indicator for on-line lithium-ion batteries remaining useful life prediction. *J. Power Sources* **2016**, *321*, 1–10. [[CrossRef](#)]
51. Wu, J.; Zhang, C.; Chen, Z. An online method for lithium-ion battery remaining useful life estimation using importance sampling and neural networks. *Appl. Energy* **2016**, *173*, 134–140. [[CrossRef](#)]

52. Ju, F.; Du, W.; Zhuang, W.C.; Li, B.; Wang, T.; Wang, W.; Ma, H. Profit-Effective Component Sizing for Electric Delivery Trucks with Dual Motor Coupling Powertrain. *Energy* **2024**, *296*, 131055. [[CrossRef](#)]
53. Liu, H.C. *Research on Prediction of Remaining Useful Life of Lithium-Ion Battery Based on Improved Neural*; Jilin University: Jilin, China, 2021.
54. Pan, H.H.; Lu, Z.Q.; Fu, B.; Wei, H.; Chen, L. Online Estimation of Lithium-ion Battery's State of Health Using Extreme Learning Machine. *Automot. Eng.* **2017**, *39*, 1375–1381,1396.
55. Wang, P.; Fan, L.F.; Cheng, Z. A Joint State of Health and Remaining Useful Life Estimation Approach for Lithium-ion Batteries Based on Health Factor Parameter. *Proc. CSEE* **2022**, *42*, 1523–1534.
56. He, Y.; Bai, W.; Wang, L.; Wu, H.; Ding, M. SOH estimation for lithium-ion batteries: An improved GPR optimization method based on the developed feature extraction. *J. Energy Storage* **2024**, *83*, 110678. [[CrossRef](#)]
57. Peng, S.; Sun, Y.; Liu, D.; Yu, Q.; Kan, J.; Pecht, M. State of health estimation of lithium-ion batteries based on multi-health features extraction and improved long short-term memory neural network. *Energy* **2023**, *282*, 128956. [[CrossRef](#)]

Disclaimer/Publisher's Note: The statements, opinions and data contained in all publications are solely those of the individual author(s) and contributor(s) and not of MDPI and/or the editor(s). MDPI and/or the editor(s) disclaim responsibility for any injury to people or property resulting from any ideas, methods, instructions or products referred to in the content.